

Experimental and Theoretical Studies on α - In_2Se_3 at High Pressure

Rosario Vilaplana,^{*,†} Samuel Gallego Parra,[‡] Alejandro Jorge-Montero,[§] Plácida Rodríguez-Hernández,[§] Alfonso Munoz,[§] Daniel Errandonea,^{||} Alfredo Segura,^{||} and Francisco Javier Manjón[†]

[†]Centro de Tecnologías Físicas, Universitat Politècnica de València, 46022 Valencia, Spain

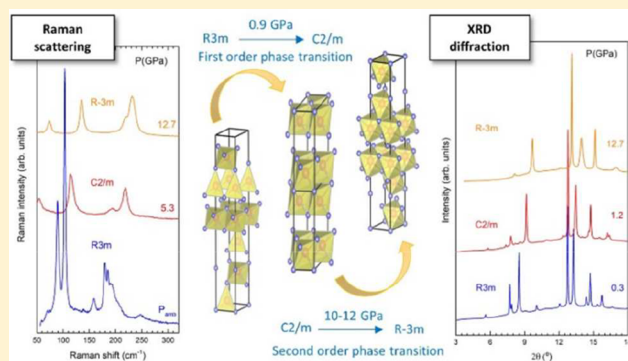
[‡]Instituto de Diseño para la Fabricación y Producción Automatizada, Universitat Politècnica de València, 46022 Valencia, Spain

[§]Departamento de Física, Instituto de Materiales y Nanotecnología, MALTA Consolider Team, Universidad de La Laguna, 38207 San Cristóbal de La Laguna, Spain

^{||}Departamento de Física Aplicada-ICMUV, MALTA Consolider Team, Universidad de Valencia, Edificio de Investigación, C/Dr. Moliner 50, 46100 Burjassot, Spain

Supporting Information

ABSTRACT: $\alpha(\text{R})$ - In_2Se_3 has been experimentally and theoretically studied under compression at room temperature by means of X-ray diffraction and Raman scattering measurements as well as by *ab initio* total-energy and lattice-dynamics calculations. Our study has confirmed the $\alpha(\text{R}3m) \rightarrow \beta'(\text{C}2/m) \rightarrow \beta(\text{R}\bar{3}m)$ sequence of pressure-induced phase transitions and has allowed us to understand the mechanism of the monoclinic $\text{C}2/m$ to rhombohedral $\text{R}\bar{3}m$ phase transition. The monoclinic $\text{C}2/m$ phase enhances its symmetry gradually until a complete transformation to the rhombohedral $\text{R}\bar{3}m$ structure is attained above 10–12 GPa. The second-order character of this transition is the reason for the discordance in previous measurements. The comparison of Raman measurements and lattice-dynamics calculations has allowed us to tentatively assign most of the Raman-active modes of the three phases. The comparison of experimental results and simulations has helped to distinguish between the different phases of In_2Se_3 and resolve current controversies.



1. INTRODUCTION

Indium selenide (In_2Se_3), a semiconductor with a direct bandgap of 1.45 eV,¹ has led to plenty of studies for decades mainly focused on its multiple applications as thermoelectric material,^{2,3} phase random access memories,^{4–6} photodetectors,^{7,8} solar cells,⁹ ferroelectricity,^{10,11} and anisotropic photoconductivity.^{12,13} Furthermore, it has been studied in the context of 2D materials, like graphene, and promising novel materials, like topological insulators (TIs).^{14,15} In this regard, A_2B_3 -type chalcogenides have recently attracted scientific interest since some of them are 3D TIs, like α - Sb_2Te_3 , α - Bi_2Se_3 , α - Bi_2Te_3 , and SnBi_2Te_4 whose vibrational properties have been studied at high pressure.^{16–19}

In_2Se_3 is a polymorphic compound with at least five known stable and three metastable phases. Like many $\text{A}^{\text{III}}_2\text{B}^{\text{VI}}_3$ compounds, some of these phases contain cation vacancies and can be classified depending on how vacancies are arranged in the unit cell. In particular, vacancies occur in structures where cations only have 4-fold coordination because the sp^3 hybridization of cation atoms imposes that the octet rule is satisfied only if 1/3 of cation positions remain unoccupied.²⁰ In this way, In_2Se_3 has layered phases without vacancies (α , β' ,

and β) and other phases with vacancies (γ , δ , κ , α' , and γ').^{21–39} The α - In_2Se_3 phase is the stable phase at room conditions;^{23–25} however, it has been reported that there are two α phases at ambient conditions: a rhombohedral $\alpha(\text{R})$ phase and an hexagonal $\alpha(\text{H})$ phase. Moreover, it has been discussed at length whether the $\alpha(\text{R})$ phase belongs to the noncentrosymmetric rhombohedral space group (S.G.) $\text{R}3m$ or to the centrosymmetric rhombohedral S.G. $\text{R}\bar{3}m$. On the other hand, the hexagonal $\alpha(\text{H})$ phase was mainly suggested to correspond to S.G. $\text{P}6_3/\text{mmc}$, but the atomic parameters of this structure have not been solved yet.^{24,26,27}

The reason for the discrepancy in the $\alpha(\text{R})$ phase between the S.G. $\text{R}3m$ and $\text{R}\bar{3}m$ resides in the difficulty of powder X-ray diffraction (XRD) measurements to distinguish between both S.G.s. To resolve this controversy, Raman scattering (RS) measurements were carried out; however, it is not easy to perform RS measurements because of the extraordinary high sensitivity of In_2Se_3 , like many other chalcogenides that are good for phase change memories, to laser light. In this regard,

Received: March 23, 2018

Published: June 26, 2018

several papers reporting RS measurements at room conditions have been published,^{30–33,35,36} but there are no clear conclusions about the nature of the $\alpha(R)$ phase since there is a lack of theoretical calculations to compare with experimental data.

It is important to know the different arrangements of In and Se atoms in the different In_2Se_3 polytypes and to understand their different properties and their behavior at high temperatures and pressures in order to optimize the multiple applications of this interesting material. It is noteworthy that the layered tetradymite (S.G. $R\bar{3}m$) structure of the β phase of In_2Se_3 has been found at room conditions in many compounds showing 3D TI properties, such as $\alpha\text{-Sb}_2\text{Te}_3$, $\alpha\text{-Bi}_2\text{Se}_3$, $\alpha\text{-Bi}_2\text{Te}_3$, and SnBi_2Te_4 . In fact, in all these layered compounds, where layers are formed by quintuple ($\alpha\text{-Sb}_2\text{Te}_3$, $\alpha\text{-Bi}_2\text{Se}_3$, $\alpha\text{-Bi}_2\text{Te}_3$) or septuple (SnBi_2Te_4) atomic layers, the $R\bar{3}m$ phase is composed of regular octahedral units around the cation in the binary compounds and around the Sn cation in the ternary compound.^{40,41}

In the last years, the high-pressure (HP) behavior of $\alpha\text{-In}_2\text{Se}_3$ has attracted considerable interest. A sequence of pressure-induced phase transitions: $\alpha \rightarrow \beta' \rightarrow \beta \rightarrow$ defective cubic Th_3P_4 at 0.8, 5.0, and 32 GPa, respectively, was reported on the basis of powder HP-XRD measurements.³⁹ Additionally, HP-RS measurements found a phonon with a negative pressure coefficient in the β ($R\bar{3}m$) phase.³⁹ Curiously, this soft phonon was not observed in two previous HP-RS studies that, in turn, did not identify the intermediate β' phase between the α and β phases.^{42,43} In this context, it is worthy to note that HP-RS studies of vibrational properties of the tetradymite phase of $\alpha\text{-Sb}_2\text{Te}_3$, $\alpha\text{-Bi}_2\text{Se}_3$, and $\alpha\text{-Bi}_2\text{Te}_3$ have not reported any experimental or theoretical soft mode in the $R\bar{3}m$ phase.⁴⁰ Additionally, a HP study has revealed a superconductivity enhancement in $\alpha\text{-In}_2\text{Se}_3$ under compression when it undergoes the transition to the defective cubic Th_3P_4 structure.⁴⁴ Finally, a recent HP study has also reported the transition from $\gamma\text{-In}_2\text{Se}_3$ to $\beta\text{-In}_2\text{Se}_3$ under compression.⁴⁵

In order to shed light into: (i) the nature of the $\alpha(R)$ phase; (ii) the existence of an intermediate β' phase between α and β phases; and (iii) the presence of a soft phonon in the β phase, we performed *ab initio* calculations of In_2Se_3 with $R3m$, $C2/m$, and $R\bar{3}m$ structures. We found that our calculations did not support the existence of a soft phonon in the β ($R\bar{3}m$) phase. This result made us suspect that laser heating could be locally damaging the sample used in ref 39, thus generating nanoclusters of selenium, which exhibit soft phonons, as previously reported in other selenides.⁴⁶ Therefore, we have revisited in this work the behavior of $\alpha\text{-In}_2\text{Se}_3$ at HP by conducting HP-XRD and HP-RS measurements at room temperature and *ab initio* total-energy and lattice-dynamics calculations up to 20 GPa. Table 1 presents the main details of the α , β' , and β phases of In_2Se_3 involved in this work.^{21,23,24,31,37–39} In sections 2 and 3, we show the experimental and theoretical details. In section 4, we show

the HP results of XRD and RS measurements and of *ab initio* calculations. In section 5, we discuss the mechanism involved in the $C2/m$ to $R3m$ phase transition and comment on the previous difficulties in observing the intermediate β' phase. Finally, in section 6 we summarize our results and provide some conclusions. We also show that our RS measurements provide clear evidence that the $\alpha(R)$ phase is the non-centrosymmetric $R3m$ phase. Furthermore, our experimental and theoretical results provide clear evidence that there is an intermediate β' phase with monoclinic $C2/m$ symmetry between the α ($R3m$) and β ($R\bar{3}m$) phases. Moreover, the β' -to- β phase transition is of second-order and takes place above 10 GPa. Finally, we show that upon hydrostatic compression the sample likely reverts to the original phase on decompression, but with considerable disorder likely due to the strong first-order character of the α -to- β' phase transition.

2. EXPERIMENTAL DETAILS

$\alpha\text{-In}_2\text{Se}_3$ powders used in this work are commercial In_2Se_3 powders purchased from Alfa Aesar Company (99.99%). In XRD and RS experiments, the samples were loaded in a DAC with a 4:1 methanol–ethanol mixture as a pressure-transmitting medium. The culet-size of the diamond anvils was 500 μm . We used an Inconel gasket, preindented to 50 μm , in which we drilled a 250 μm diameter hole. The 4:1 methanol–ethanol mixture is hydrostatic up to 10 GPa and quasi-hydrostatic up to the maximum pressure reached in our experiments.⁴⁷ In addition, we took precautions to minimize the deviatoric stresses induced in the experiments during the DAC loading.⁴⁸

HP-XRD measurements at room temperature up to 25 GPa were conducted at the BL04-MSPD beamline of ALBA synchrotron using the equation of state of copper powder mixed with the sample to determine the pressure inside the DAC. An incident monochromatic beam with wavelength of 0.4246 Å was focused to $20 \times 20 \mu\text{m}$.⁴⁹ Images covering a 2θ range up to 20° were collected using a Rayonix SX165 CCD located at 240 mm from the sample. One-dimensional diffraction profiles of intensity as a function of 2θ were obtained by integration of the observed intensities with the Fit2D software.⁵⁰ Rietveld refinements were carried out with GSAS package software.⁵¹ The equation of state (EOS) of copper was used for pressure calibration.⁵²

HP-RS measurements were performed with a LabRAM HR UV microspectrometer coupled to a Peltier cooled CCD camera, using a 532 nm solid state laser excitation line with a power smaller than 1 mW and a spectral resolution better than 2 cm^{-1} . In order to be sure that no heating effects occur during the measurements, the sample was checked during all Raman experiments. Concerning the analysis of Raman spectra under pressure, Raman peaks have been fitted to Voigt profiles (Lorentzian profile convoluted by a Gaussian profile) where the spectrometer resolution is taken as the fixed Gaussian width. As already commented, two HP runs were performed in In_2Se_3 in order to obtain the spectra of the first phase since the transition is about 0.8 GPa. The pressure was determined by the ruby luminescence method;⁵³ the shape and separation of the R1 and R2 ruby lines were checked at each pressure, and neither a significant increase in width nor an overlapping of both peaks were detected.

3. SIMULATION DETAILS

Structural and vibrational data were obtained by means of *ab initio* total-energy and lattice-dynamics calculations in the framework of density functional theory (DFT).⁵⁴ This method allows an accurate description of the physical properties of semiconductors at HP.⁵⁵ The simulations were conducted with the Vienna *Ab Initio Simulation Package* (VASP).⁵⁶ The projector-augmented wave scheme (PAW)⁵⁷ was employed to take into account the full nodal character of the all-electron charge density in the core region. The plane waves basis set was extended to a cut off of 320 eV in order to have accurate results.

Table 1. Crystal Structure, S.G., and Number of α , β' , and β Phases

Phase	Crystal structure	S.G.	Number	refs
α	Rhombohedral	$R3m$	160	23, 24, 31
β'	Monoclinic	$C2/m$	12	37–39
β	Rhombohedral	$R\bar{3}m$	166	21, 23, 24

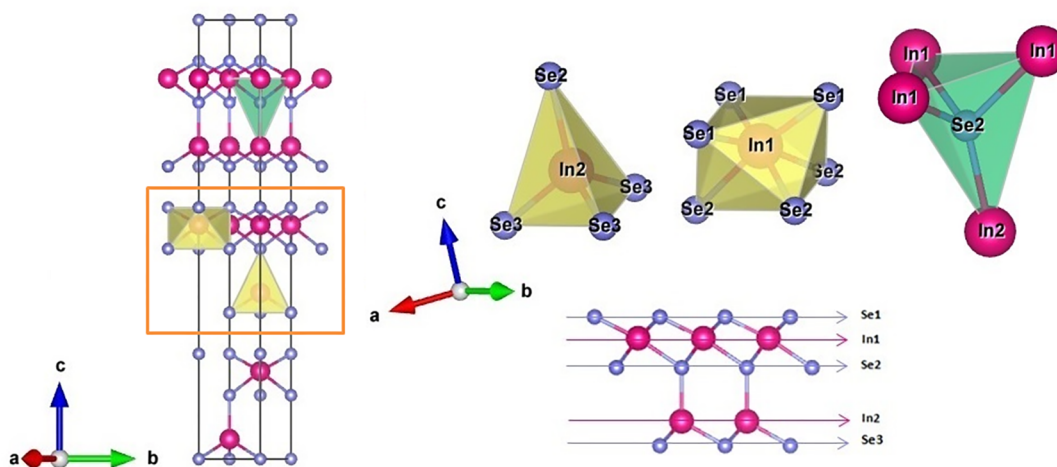


Figure 1. Detail of the structure of the α In_2Se_3 phase. Right bottom corner: quintuple layer. Right top corner: three polyhedra centered in In2, In1, and Se2 atoms.

The exchange-correlation energy was described in the generalized-gradient approximation (GGA) with the Perdew–Burke–Ernzenhof prescription.⁵⁸ For each of the studied phases, integrations within the Brillouin zone (BZ) were performed with dense meshes of Monkhorst–Pack k -special points. In this way, a high convergence of 1 meV per formula unit was accomplished. At a set of selected volumes, the lattices parameters and atomic positions were fully optimized by calculating the forces on the atoms and the stress tensor. In the optimized resulting structures, the forces on the atoms were lower than 0.002 eV/Å and the deviation of the stress tensor components from the diagonal hydrostatic form was less than 0.1 GPa. In our simulations, after the relaxation process of the considered structure, we obtain a set of energies and volumes at different pressures.⁵⁹

Lattice-dynamic calculations were carried out at the center of the Brillouin zone (Γ point). The direct force-constant approach (or supercell method)⁶⁰ was employed. This method requires highly converged results on forces. The diagonalization of the dynamical matrix determines the frequencies of Raman- and infrared-active modes. From the calculations, the symmetries of the eigenvectors of the different vibrational modes are also identified at the Γ point.

4. RESULTS

4.1. HP-XRD Measurements. The α ($R3m$) structure of In_2Se_3 can be visualized as a layered structure composed of quintuple layers (Se–In–Se–In–Se) that are linked by weak van der Waals forces (see Figure 1). In this structure, there are five inequivalent atoms occupying 3a Wyckoff sites (In1, In2, Se1, Se2, and Se3). The two inequivalent In1 and In2 atoms have 6-fold and 4-fold coordination, respectively. The three inequivalent Se atoms also have different coordinations. The Se atom in the center of the layer (Se2) is 4-fold coordinated to three In1 and one In2 atoms, forming a distorted tetrahedron, while Se atoms at the layer surface (Se1 and Se3) have a 3-fold coordination. However, Se1 atoms linked to In1 atoms show bond distances above 2.7 Å at room pressure, while Se3 atoms linked to In2 atoms show smaller bond distances below 2.7 Å at room pressure.

HP-XRD measurements on powder samples were performed up to 20.2 GPa as shown in Figure 2. XRD patterns below 0.5 GPa can be indexed with the α ($R3m$) phase, while those above 1.2 GPa can be indexed with the β' phase. At 11.9 GPa, the XRD pattern can still be properly assigned to the β phase; however, patterns above 12.7 GPa can only be indexed with the β phase. Our results are in good agreement with those of

ref 39, thus confirming the existence of the intermediate β' phase between α and β phases. The only difference with respect to ref 39 is the pressure at which we locate the $\beta' \rightarrow \beta$ transition. One of the main characteristics of this transition is the merging of several Bragg peaks near $2\theta = 15^\circ$ (they correspond to a d -spacing in the range 1.68–1.52 Å as shown in Figure S1 of the Supporting Information). Zhao et al. pointed at this merging as the indication of the $\beta' \rightarrow \beta$ transition at 5 GPa.³⁹ However, the merging of the two peaks into a single one is smooth and keeps on up to higher pressures, making it difficult to accurately determine the transition pressure. In addition to the peak merging, there are additional changes in the XRD pattern that help to determine more accurately the transition pressure. In particular, a weak peak present at 11.9 GPa (see inset of Figure 2), but disappearing at 12.7 GPa, can be indexed with the β' phase and not with the β phase. Moreover, the R -values of the Rietveld refinements are smaller for the β' phase than for the β phase at all pressures from 1.2 to 11.9 GPa, as was also found in previous examples of two phases linked by a group–subgroup relationship.^{61–63} We consider that this evidence supports that the transition pressure is around 12.7 GPa and not around 5.0 GPa as previously assigned.³⁹ The gradual transformation of β' phase into β phase and the fact that there is no volume discontinuity suggests that the $\beta' \rightarrow \beta$ phase transition is a second-order transformation,⁶⁴ as the one observed under compression in the related compound InSe .⁶⁵ We will show below that these conclusions are supported by our HP-RS measurements and *ab initio* calculations.

For the sake of completeness, we show in Figure 3 the pressure evolution of the experimental and theoretical lattice parameters and unit cell volume in the different phases (see numerical data in Table S1 of the Supporting Information). As observed, the change in volume from the α phase at 0.5 GPa ($399 \text{ Å}^3 \rightarrow V/Z = 133 \text{ Å}^3$) to the β' phase at 1.2 GPa ($248.7 \text{ Å}^3 \rightarrow V/Z = 124.35 \text{ Å}^3$) implies a relative change $\Delta V/V = 6\%$. Note that an extrapolation of the α phase up to 1.2 GPa would yield a $\Delta V/V = 4\%$ which is in good agreement with ref 39. On the other hand, the change in volume from the β' phase at 11.9 GPa ($216.3 \text{ Å}^3 \rightarrow V/Z = 108.15 \text{ Å}^3$) to the β phase at 12.7 GPa ($319.9 \text{ Å}^3 \rightarrow V/Z = 106.63 \text{ Å}^3$) results in a $\Delta V/V = 1\%$. If we extrapolate the β' phase up to 12.7 GPa, then we obtain a $\Delta V/V = 0\%$, which agrees with the second-order character of

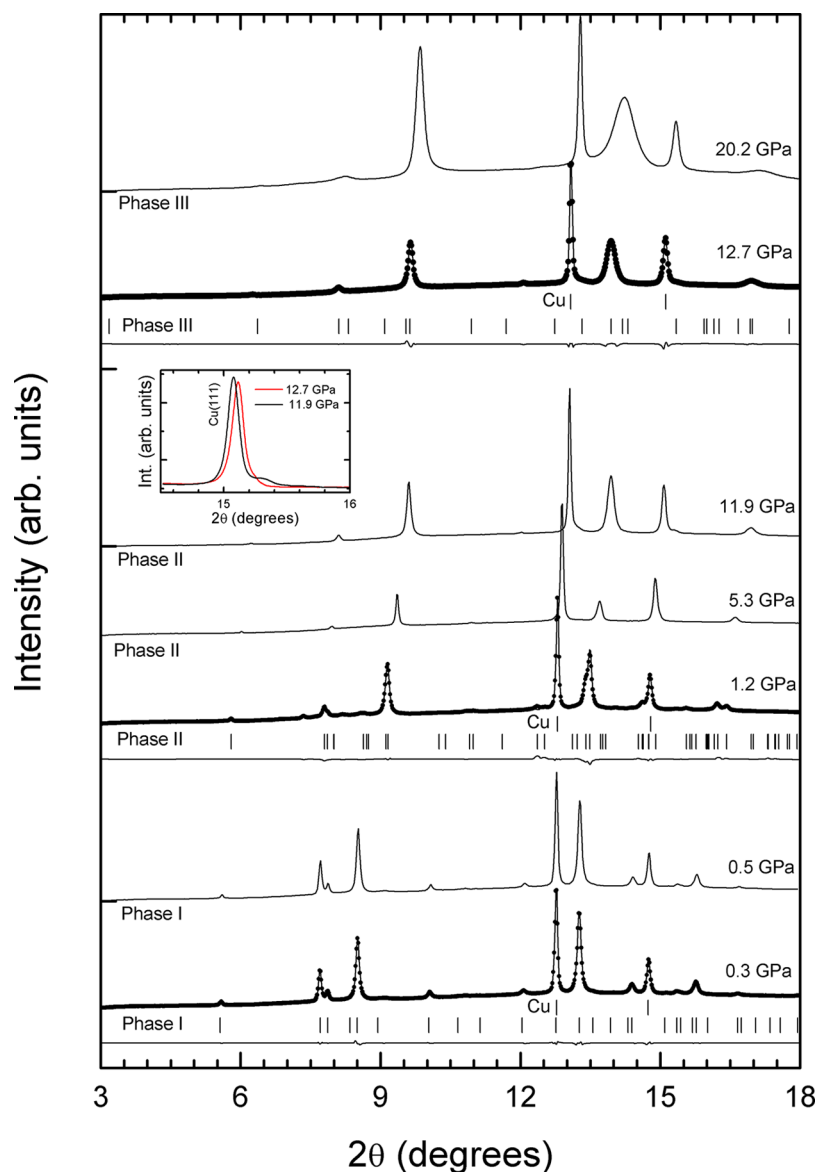


Figure 2. HP-XRD patterns at selected pressures. Rietveld refinements are shown for: (i) phase I (rhombohedral structure, S.G. $R\bar{3}m$) at 0.3 GPa; (ii) phase II (monoclinic structure, S.G. $C2/m$) at 1.2 GPa; and (iii) phase III (rhombohedral structure, S.G. $R\bar{3}m$) at 12.7 GPa. Experimental data are plotted as solid lines, calculated profiles as circles, and residuals are also shown by solid lines in the bottom part of the refined patterns. The background has been removed from all XRD patterns. Vertical ticks indicate the position of Bragg reflections as well as the vertical ticks up indicate the position of copper reflections. The inset shows the small changes associated to the conclusion of the second-order phase transition.

the β' – β phase transition, as suggested in ref 39. As regards the α phase, it can be observed that there is a slightly larger compression of the experimental c lattice parameter and the volume than of the theoretical one. We think that this small difference is due to the fact that DFT calculations tend to overestimate compression for the van der Waals interaction between the layers. In any case, there is a rather good agreement between our experimental and theoretical values.

We have used a second-order Birch–Murnaghan state equation in order to obtain the parameters at room pressure for α , β' , and β phases of In_2Se_3 and to compare them with those reported in ref 39 (see Table 2). As can be seen in Table 2, the bulk moduli of phase I and II are underestimated in ref 39. The underestimation of the bulk moduli in ref 39 can be caused by the fact that data points for the pressure region where phase coexistence is observed have been included in the EOS determination. In our case, we have carefully selected

only data points for phase I where either phase I or phase II were detected as single phases, which make us confident in the EOS parameters determined in the present work.

It must be stressed that the β ($R\bar{3}m$) phase can be transformed by group–subgroup relationships into the β' ($C2/m$) phase. In fact, $C2/m$ is a translationengleiche subgroup of $R\bar{3}m$. This means that if some geometrical relations are satisfied by the unit-cell parameters in the β' phase, the β' phase can be reduced to the higher symmetry β phase. The relations are $a_m = 2b_m \sin 120^\circ$ and $\beta = \sin^{-1}(\frac{1}{4}) + 90^\circ = 104.4775^\circ$, where a_m , b_m , and β are unit-cell parameters of β' . Under these conditions, the monoclinic β' structure becomes the rhombohedral β structure. The unit-cells of both structures are related by $a_r = b_m$ and $c_r = 3c_m \sin \beta$, where subindexes r and m refer to the rhombohedral and monoclinic structures. From the analysis of

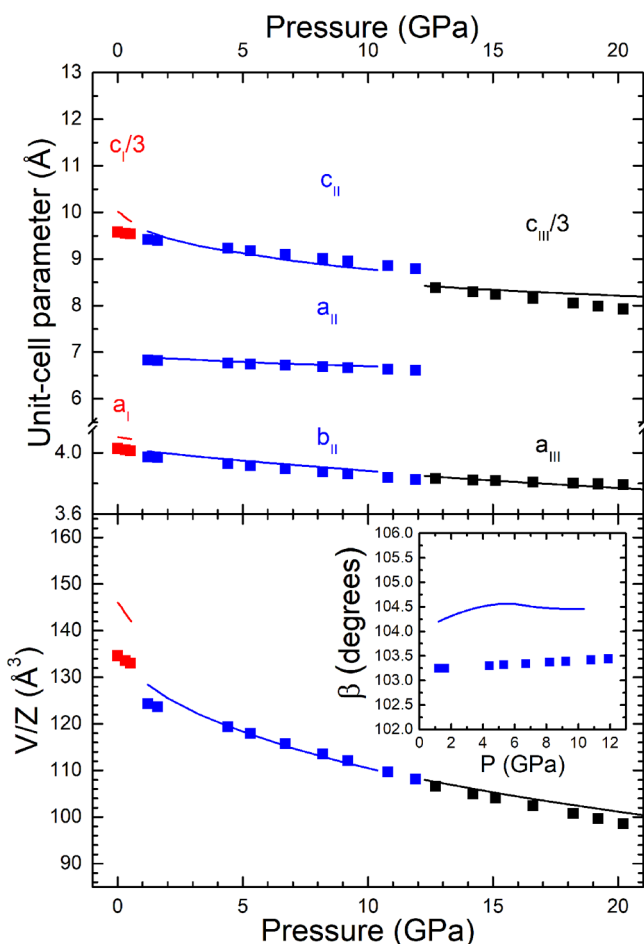


Figure 3. Pressure dependence of the experimental (symbols) and theoretical (line) lattice parameters and unit cell volume of the α , β' , and β phases in In_2Se_3 . The inset shows the pressure dependence of the monoclinic β angle.

Table 2. Parameters of Second-Order Birch-Murnaghan Equation of State at Ambient Pressure Obtained for α , β' , and β Phases of In_2Se_3 and Its Comparison with a Previous Study

	Phase I	Phase II	Phase III	
V_0 (\AA^3)	403.8(5)	256(1)	375(2)	This work
B_0 (GPa)	40(2)	48(4)	60(6)	
V_0 (\AA^3)	407.9	260.1	369.8	ref 39
B_0 (GPa)	31	35	66	

the pressure dependence determined for the β' phase, we confirmed that the “magic” relation between the unit-cell parameters that transform β' into β in In_2Se_3 is achieved only at 12.7 GPa.

4.2. HP-RS Measurements. As already mentioned, a Raman mode with a negative pressure coefficient was observed in previous HP-RS measurements on $\alpha\text{-In}_2\text{Se}_3$,³⁰ which was not observed in other HP studies.^{31,32} In this context, we want to stress that the appearance of soft phonons attributed to the formation of a nanocluster of Se atoms because of the local decomposition of the In_2Se_3 sample were previously observed.³³ Therefore, we assumed that the observation of a soft phonon in previous HP-RS measurements of In_2Se_3 could evidence thermal degradation of the sample by laser heating and could provide a distorted understanding of the pressure

effects on $\alpha\text{-In}_2\text{Se}_3$. Consequently, we decided to repeat HP-RS measurements in $\alpha\text{-In}_2\text{Se}_3$ by taking into account the strong sensitivity of this material to laser light. In this way, we could compare RS measurements with lattice dynamics calculations as a check to verify the goodness of our HP-RS measurements and calculations and also in order to understand why in previous HP-RS experiments^{42,43} the β' phase was not identified.

The irreducible representations of the Raman active phonons at Γ for the three phases α ($R3m$), β' ($C2/m$), and β ($R\bar{3}m$) phases (see Table 3) show that there are eight, six,

Table 3. Irreducible Representations of the Raman Active Phonons in Γ for the α , β' , and β Phases

Phase	Raman-active modes in the center zone Γ
α	$\bar{\Gamma} = 4A_1 + 4E$
β'	$\bar{\Gamma} = 4A_g + 2B_g$
β	$\bar{\Gamma} = 2A_{1g} + 2E_g$

and four Raman-active modes corresponding to the α , β' , and β phases, respectively. However, since the α phase is noncentrosymmetric, all Raman-active modes are also infrared-active and a TO-LO splitting could be observed.²⁷

Figure 4 shows the RS spectra of In_2Se_3 compressed up to 20 GPa. As observed, there is no phonon mode that softens

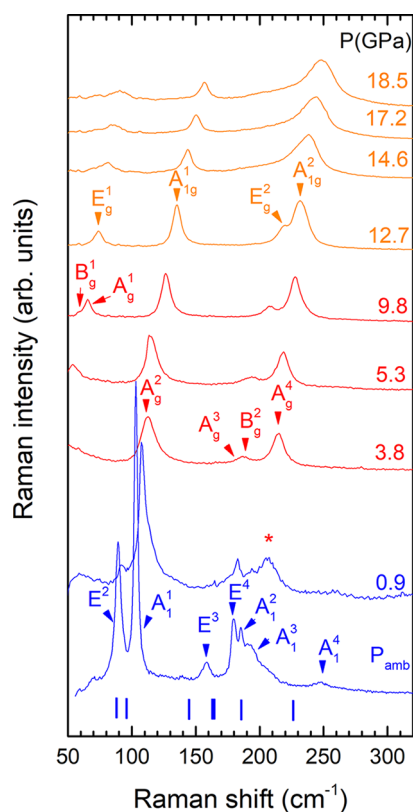


Figure 4. HP-RS spectra at different pressures. Spectra corresponding to α , β' , and β phases are shown in blue, red, and orange, respectively.

under pressure in the whole range of pressures studied. This result is in agreement with refs 42 and 43 and in contrast to ref 39. In the RS spectrum at room pressure, all modes of the initial phase are indicated with arrows, with the exception of the E^1 mode whose frequency is below our spectrometer range.

Unfortunately, most of the modes are overlapped, so we show in Figure S2 a detailed view with all resolved modes of α phase. A comparison of the pressure dependence of the experimental and theoretical Raman-active mode frequencies of α -In₂Se₃ is shown in Figure 5. A good agreement is found between

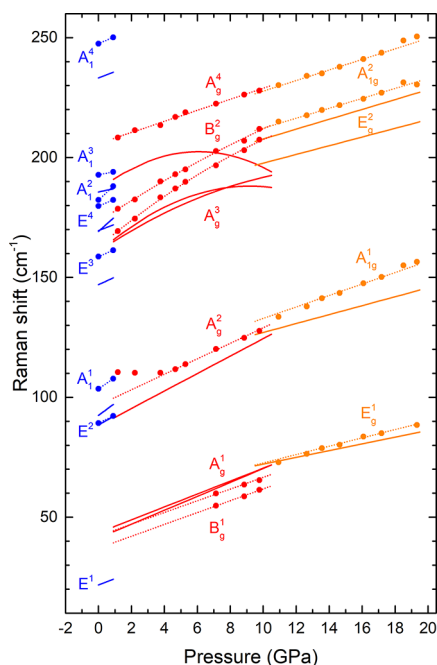


Figure 5. Pressure dependence of the experimental (symbols) and theoretical (lines) Raman-active mode frequencies of the α , β' , and β phases in blue, red, and orange, respectively. Short dotted lines represent fitted experimental Raman modes.

experimental and theoretical frequencies and pressure coefficients for this phase, with no soft phonon either in RS measurements or in calculations.

Our HP-RS measurements show that the transition to β' phase occurs about 0.9 GPa because the RS spectrum at that pressure shows clearly the modes of the α phase with a new peak which corresponds to the next phase (see the asterisk symbol in Figure 4). This indicates the onset of the transition to the new phase. We have adjusted the shape of the Raman peaks with pseudo-Voigt functions and in this way we have been able to resolve the two peaks that we have tentatively assigned to the A_g^3 and B_g^2 modes (see RS spectrum at 3.8 GPa) and, later, those assigned to the A_g^1 and B_g^1 (see RS spectrum at 9.8 GPa) of the β' phase. For more information, resolved A_g^3 and B_g^2 modes at 3.8, 5.3, and 9.8 GPa are displayed in Figure S3. A comparison of the pressure dependence of the experimental and theoretical Raman-active mode frequencies of β' -In₂Se₃ is shown in Figure 5.

The first thing to point out is the strong similarity of the calculated modes in the β' and β phases. The A_g^1 and B_g^1 modes of the β' phase are almost overlapped and difficult to distinguish from the E_g^1 mode of the β phase. The same happens with the A_g^3 and B_g^2 modes of the β' phase and the E_g^2 mode of the β phase. On the other hand, the A_g^2 modes of the β' phase and A_{1g}^1 of the β phase are indistinguishable, as well as the A_g^4 mode of the β' phase and the A_{1g}^2 mode of the β phase. Therefore, our calculations show that both phases are very similar and provide a valuable help to understand why previous HP-RS measurements have not been able to identify

the intermediate β' phase. Between 5 and 10 GPa calculations show an abrupt decrease of the highest frequency A_g^3 mode (see Figure 5).

According to our RS measurements and calculations, the β' -to- β phase transition takes place around 10–12 GPa and not around 5.0 GPa as suggested by previous HP-XRD measurements.³⁹ In order to corroborate experimentally the pressure at which the transition to the β phase is completed, we have plotted the full width at half-maximum (fwhm) of the phonon A_g^2 in the β' phase (see Figure 6). The fwhm decreases with

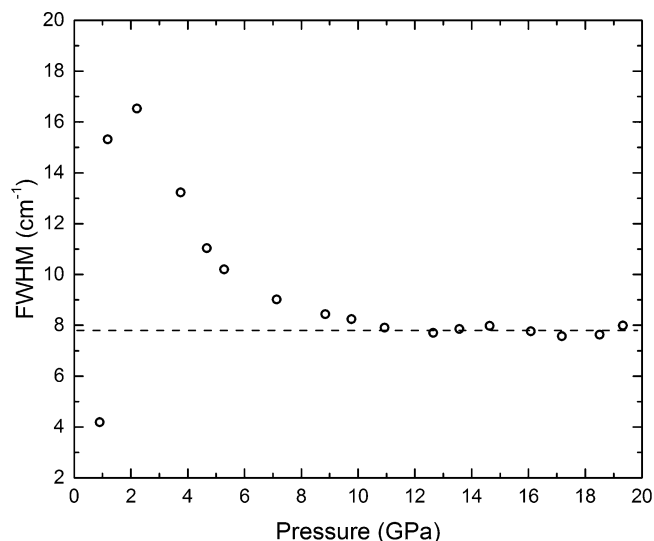


Figure 6. Pressure dependence of the fwhm of the A_g^2 mode in the β' phase, which changes to the A_{1g}^1 mode in the β phase above 10–12 GPa.

increasing pressure and stabilizes at about 10–12 GPa. Therefore, this result reinforces the fact that the transition is completed around 10–12 GPa. In other words, it seems that this process is gradual and it takes a range of pressures to be completed.

Summing up, HP-RS results and their comparison to *ab initio* calculations have allowed us to assign most of the modes of the different phases. In Tables 4, 5, and 6 we have summarized experimental and theoretical Raman mode frequencies together with their pressure coefficients for the three phases. It should be noted that the E^1 (α phase) mode is

Table 4. Experimental and Theoretical Raman-Active Mode Frequencies and Their Pressure Coefficients as Derived from a Fit to $\omega(P) = \omega_0 + a(P - P_0)$ of the α Phase ($P_0 = 0$ GPa)

Mode	$\omega_0(\text{exp})$ (cm ⁻¹)	$a(\text{exp})$ (cm ⁻¹ GPa ⁻¹)	$\omega_0(\text{th})$ (cm ⁻¹)	$a(\text{th})$ (cm ⁻¹ GPa ⁻¹)
E ¹	27 ^a		21.7	2.68
E ²	89.2	3.28	88.5	3.85
A ₁ ¹	103.5	4.77	92.5	5.09
E ³	158.7	2.98	147.0	3.19
E ⁴	179.8	2.80	169.5	2.69
A ₂ ¹	182.3	6.36	169.2	6.16
A ₃ ¹	192.8	1.33	185.6	1.42
A ₄ ¹	247.5	2.98	233.2	2.71

^aThis E-type mode was observed in ref 26 in good agreement with our theoretical data.

Table 5. Experimental and Theoretical Raman-Active Mode Frequencies of the β' Phase and Their Pressure Coefficients Derived from a Primer Order Fit $\omega(P) = \omega_0 + a(P - P_0)$ or to $\omega(P) = \omega_0 + a(P - P_0) + b(P - P_0)^2$ ($P_0 = 0.9$ GPa)

Mode	$\omega_0(\text{exp})$ (cm^{-1})	$a(\text{exp})$ ($\text{cm}^{-1} \text{ GPa}^{-1}$)	$b(\text{exp}) \times 100$ ($\text{cm}^{-1} \text{ GPa}^{-1}$)	$\omega_0(\text{th})$ (cm^{-1})	$a(\text{th})$ ($\text{cm}^{-1} \text{ GPa}^{-1}$)	$b(\text{th}) \times 100$ ($\text{cm}^{-1} \text{ GPa}^{-1}$)
B_g^1	39.3	2.47		43.9	2.90	
A_g^1	44.4	2.44		45.9	2.69	
A_g^2	99.9	3.23		91.3	3.65	
B_g^2	177.3	4.43	−6.8	164.9	4.31	−14.9
A_g^3	167.9	5.54	−13.1	165.6	5.41	−32.6
A_g^4	207.9	2.3		190	4.46	−43

Table 6. Experimental and Theoretical Raman-Active Mode Frequencies of the β Phase and Their Pressure Coefficients as Derived from a Fit to $\omega(P) = \omega_0 + a(P - P_0)$ or to $\omega(P) = \omega_0 + a(P - P_0) + b(P - P_0)^2$ ($P_0 = 10$ GPa)

Mode	$\omega_0(\text{exp})$ (cm^{-1})	$a(\text{exp})$ ($\text{cm}^{-1} \text{ GPa}^{-1}$)	$\omega_0(\text{th})$ (cm^{-1})	$a(\text{th})$ ($\text{cm}^{-1} \text{ GPa}^{-1}$)
E_g^1	72.6	1.74	72.1	1.41
A_{1g}^1	132.9	2.39	127.1	1.86
E_g^2	212.3	2.07	197.7	1.81
A_{1g}^2	227.7	2.20	207.7	2.05

not observed in our setup owing to their low frequency. The same happens with the B_g^1 and A_g^1 (β' phase) which can be observed at about 7.0 GPa. Note that the A_g^4 (β' phase) mode is the only one whose pressure dependence is different in experiment and calculations. At present, we have no explanation for this fact as well as for the rather large difference between some experimental and theoretical absolute frequencies. In Figure S4 of the Supporting Information, we show the RS data on downstroke. Despite the difficulty on the discrimination between β' and β phases due to the second-order character of this phase transition, we can appreciate by looking at the A_{1g}^1 mode of the β phase a sign of the back transformation to the A_g^2 mode of the β' phase. Note that this mode becomes more intense and defined below 10 GPa.

Finally, we must comment that the RS spectrum of the released sample appears to be that of an amorphous or disordered-like α phase since the position of the broad bands is similar to the frequencies of the Raman-active phonons in the α phase (see Figure S5). However, the RS spectrum of the released sample does not look similar to that of previous amorphous In_2Se_3 .⁶⁶ Our RS spectrum clearly reflects a similarity with the RS spectrum of the α phase while that of Weszka et al. shows much close similarity to those of Se clusters, as already commented by Weszka et al., likely due to thermal heating of their nanometer-size samples with the green and blue lasers.⁶⁶ Besides, we have to stress that our result shows the irreversibility of the compression process in α - In_2Se_3 . This makes sense if we consider that there is a considerable rearrangement of cations, especially at the $\alpha \rightarrow \beta'$ transition (7% volume reduction and “average” 5-fold to 6-fold coordination change for In atoms), and that the β' phase cannot be recovered at ambient conditions in equilibrium conditions. Note the two infrared modes (A_u^1 and B_u^1) with imaginary frequency at ambient pressure in Figure S6 of the Supporting Information. For the sake of completeness, Figure S6 shows the IR active modes obtained by our *ab initio* calculations. Interestingly, it shows a monotone progression from β' to β IR modes around 10 GPa; we even see how the two lowest β' soft IR modes coincide with the lowest IR mode of the β phase at 10 GPa. Concluding, we can say that the Raman modes of all these phases are not easy to discern,

especially those of the β' and β phases; however, we have been able to discern the phonons associated with both β' and β phases and show that the $\beta' \rightarrow \beta$ transition is completed around 10 GPa.

5. DISCUSSION

In order to shed light on the mechanisms of pressure-induced phase transitions in α - In_2Se_3 , we have plotted two images of three phases involved by using the VESTA software (see Figure 7).⁶⁷ In the images at the top, we highlight the

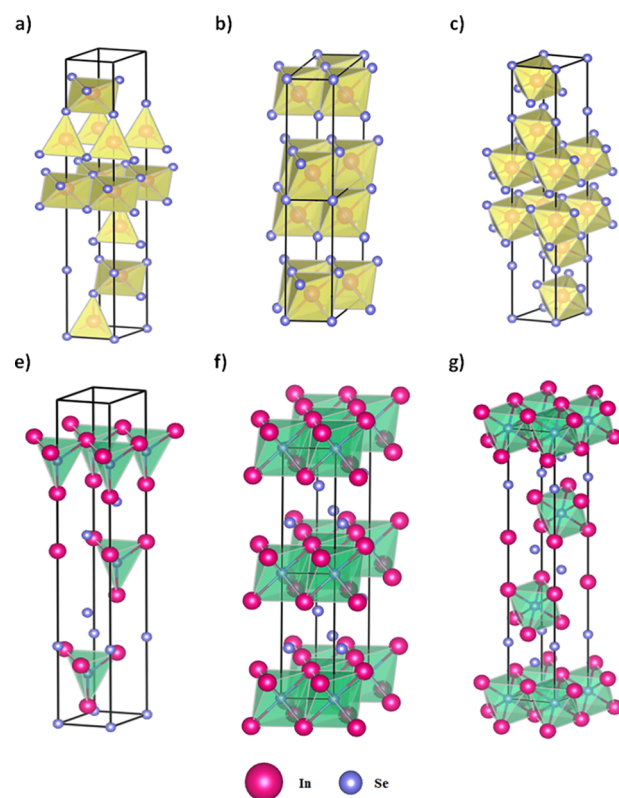


Figure 7. Schematic view of the phases of In_2Se_3 as a function of pressure. (a), (b), and (c) images show the different polyhedra associated with In atoms in the α , β' , and β phases, respectively; while (d), (e), and (f) images show the polyhedra associated with Se atoms at the center of the quintuple layers in each phase.

polyhedra associated with In atoms, while in the image at the bottom we highlight the polyhedra associated with Se atoms. From these theoretical structures, we have obtained the bond distances associated with these polyhedra as a function of pressure. Figures 8a and 8b show the evolution of the bond distances versus pressure of the polyhedra associated with the In and Se atoms of α , β' , and β phases in Figure 7.

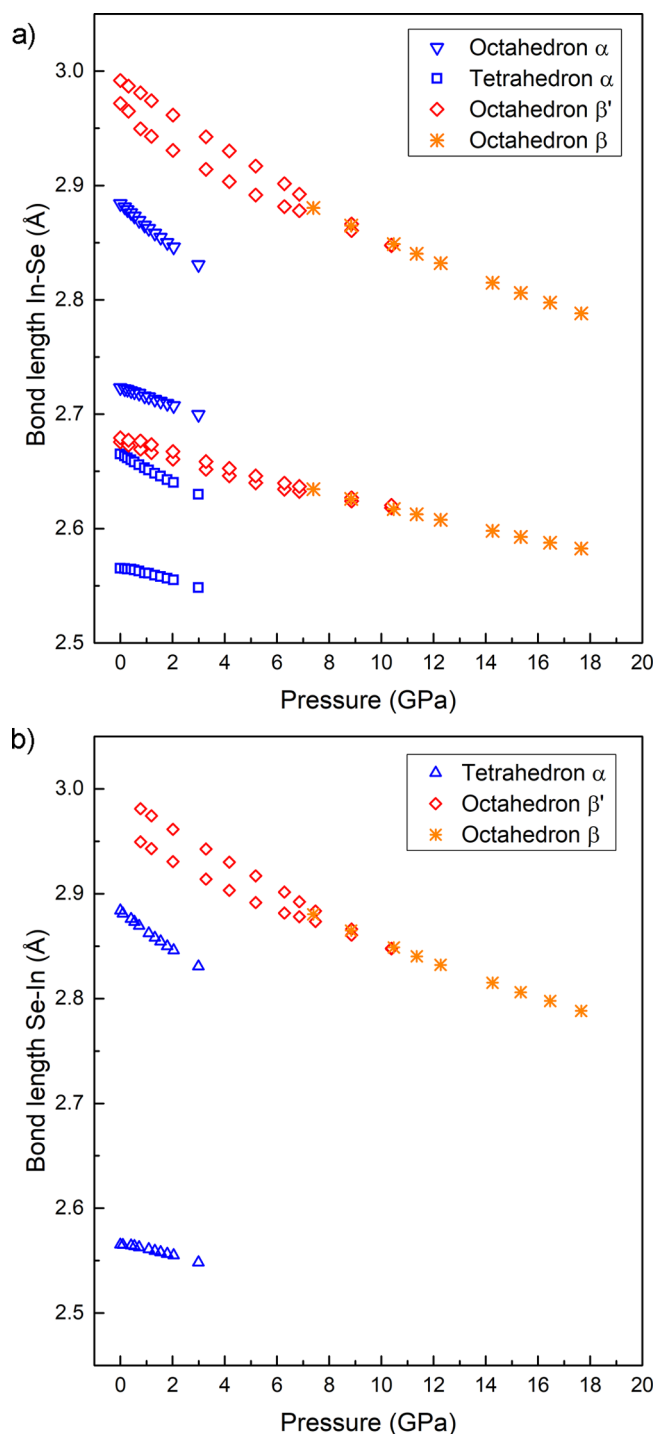


Figure 8. Pressure dependence of the In–Se bond distances for the different phases α , β' , and β . (a) In–Se distances associated with the polyhedral units around In atoms of Figure 7: α phase: octahedron (empty triangle symbol) and tetrahedron (empty square symbol); β' phase: irregular octahedron (empty rhombus symbol); β phase: regular octahedron (asterisk symbol). (b) In–Se distances associated with the polyhedral units around Se atoms of Figure 7: α phase: irregular tetrahedron (empty triangle symbol); β' phase: irregular octahedron (empty rhombus symbol); β phase: regular octahedron (asterisk symbol).

As can be seen in Figure 8a and 8b, the $\alpha \rightarrow \beta'$ phase transition implies a discontinuity in the bond distances of the polyhedra associated with In and Se atoms which highlights

the change in coordination for In and Se atoms already commented. On the other hand, Figure 9 shows two units of β'

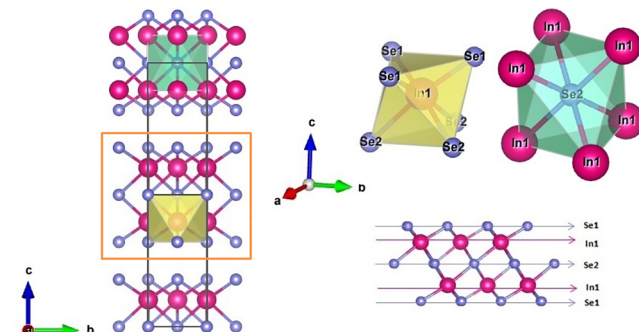


Figure 9. Detail of two unit cells of β' - In_2Se_3 . Right bottom corner: the quintuple layer. Right top corner: the two irregular octahedra associated with In and Se atoms.

phase highlighting the polyhedra associated with In and Se atoms. The quintuple block is shown at the bottom right corner. The β' phase is characterized by one irregular octahedron associated with Se atoms, in the middle of the quintuple block and another irregular octahedron associated with In atoms. These two irregular octahedra are plotted separately at the right top corner. Polyhedra associated with the In atoms have four different bond distances whereas that related to the Se atoms has only two different bond distances (see Figure 8a and 8b). It is noted that in the β' phase, the two polyhedra associated with In1 and In2 atoms (a tetrahedron and an octahedron) of the α phase become equivalent since the effective coordination number of the In1 atom increased. The polyhedron associated with the Se atom also increased its coordination. In other words, these two polyhedra become 6-fold coordinated.

In turn, the $\beta' \rightarrow \beta$ phase transition proceeds with a progressive regularization of the octahedral units associated with the In and Se atoms as pressure increases. When the transition is completed, the octahedron associated with In atoms continues being irregular but only with two different bond distances. Contrarily, the octahedron associated with the Se atom becomes completely regular (see Figures 8a and 8b). It is worthy to note that values of bond distances from about 6.0 to 9.0 GPa are very close but the transition is not completed up to approximately 10 GPa according to the calculation. This pressure again is slightly higher than that reported in the XRD experiment of Zhao in ref 39 and in accordance with our results of HP- XRD and RS.

We can conclude that the progressive regularization of the octahedra of both In and Se atoms without any discontinuity in the bond distance is an indication of the second-order character of the $\beta' \rightarrow \beta$ phase transition. The full regularization of the octahedron of the Se atom indicates the end of the transition to the $R\bar{3}m$ phase. Both β' and β phases are energetically competitive, as can be seen from the enthalpy difference versus pressure of the three phases (Figure 10). Despite these enthalpies are calculated at 0 K, the pressure values of the $\alpha \rightarrow \beta'$ and $\beta' \rightarrow \beta$ transitions are quite close to values obtained experimentally.

In Figure 11 is shown the hexagonal unit cell of β - In_2Se_3 . In addition, Figures 12a and 12b show the pressure dependence of the mean or “effective” coordination number (ECoN) of the

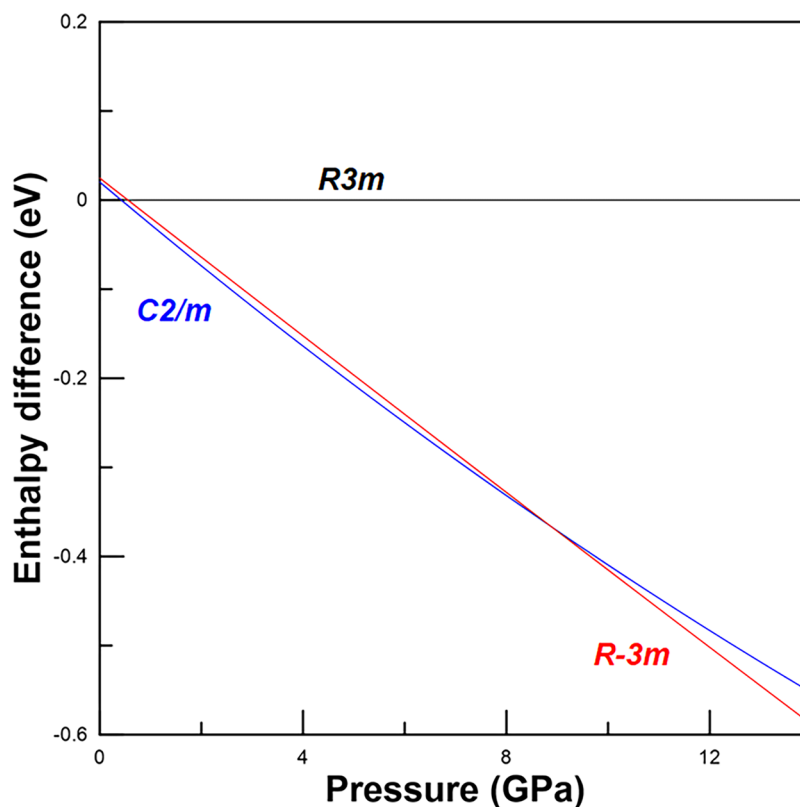


Figure 10. Enthalpy difference versus pressure at 0 K for the α , β' , and β phases of In_2Se_3 .

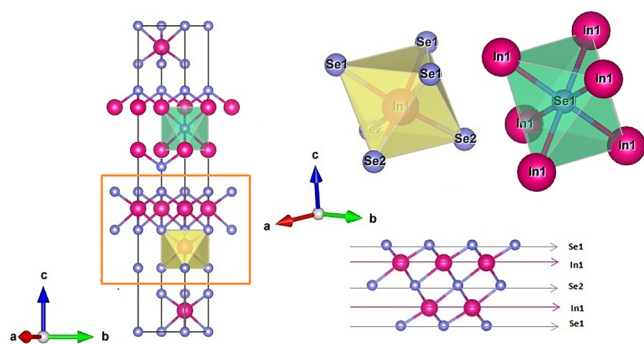


Figure 11. Detail of the hexagonal unit cell of $\beta\text{-In}_2\text{Se}_3$. Right bottom corner: quintuple layer. Right top corner: two polyhedra centered in In and Se atoms.

octahedra of In and Se atoms in the β' and β phases. Several proposals have been made for the calculation of ECoN by adding all surrounding atoms with number between 0 and 1. We have used that adopted in the VESTA software^{68–70} whose definition is given in the Supporting Information. These two figures support that the transition from β' to β phase is gradual and completed around 10 GPa. It is worthy to note that the effective coordination number of the octahedron associated with Se atoms reaches a constant value equal to 6, indicating the regularization of these octahedra and supporting that phase transition to the β phase is completed at about 10 GPa.

We have visualized in Figure 13 the atomic vibrations which are responsible for the A_g^2 (β' phase) and A_{1g}^1 (β phase) modes with the program Jmol.⁷¹ As observed, the central Se layer of quintuple layers remains fixed in them and Se and In symmetric layers compress out-plane in the A_g^2 mode of the β'

phase (Figure 13a); however, in the A_{1g}^1 mode of the β phase, they stretch the quintuple layers (Figure 13 b)).

We can conclude that the monoclinic β' phase symmetrizes gradually until it reaches a relationship of network parameters that makes the structure rhombohedral. Once it reaches the high symmetry, the structure remains stable up to the highest pressure covered by our studies. A consequence of the transition mechanism is that the nature of the transition is second-order (no volume discontinuity). The fact that the $\beta' \rightarrow \beta$ phase transition is very subtle might be the reason why Zhao et al. gave a transition pressure lower than us and why Rasmussen et al. conclude from their RS experiment that the $\alpha \rightarrow \beta$ phase transition occurs directly at about 0.7 GPa,⁴² despite XRD measurements were properly conducted. A similar conclusion was reached by Ke et al.⁴³ arguing that there is a shear shift of planes in an attempt to explain the mechanism that leads directly from the α to β phase. Such a claim is not plausible, given that, as we have seen above in the descriptions of the different phases, the α phase is formed by sheets of octahedra and tetrahedra centered at the In1 and In2 atoms while the β phase only contains octahedra associated with In atoms. Therefore, a shift of planes cannot lead from α to β . Besides, the lack of full reversibility to the α phase clearly indicates the reconstructive character of the $\alpha \rightarrow \beta'$ phase transition.

6. CONCLUSIONS

We have performed a joint experimental and theoretical study of the structural and vibrational properties of $\alpha(\text{R})\text{-In}_2\text{Se}_3$ under compression by means of X-ray diffraction and Raman scattering measurements as well as by *ab initio* total-energy and lattice-dynamics calculations. Our study has confirmed the $R3m$ nature of the $\alpha(\text{R})$ phase and the $\alpha \rightarrow \beta' \rightarrow \beta$ sequence

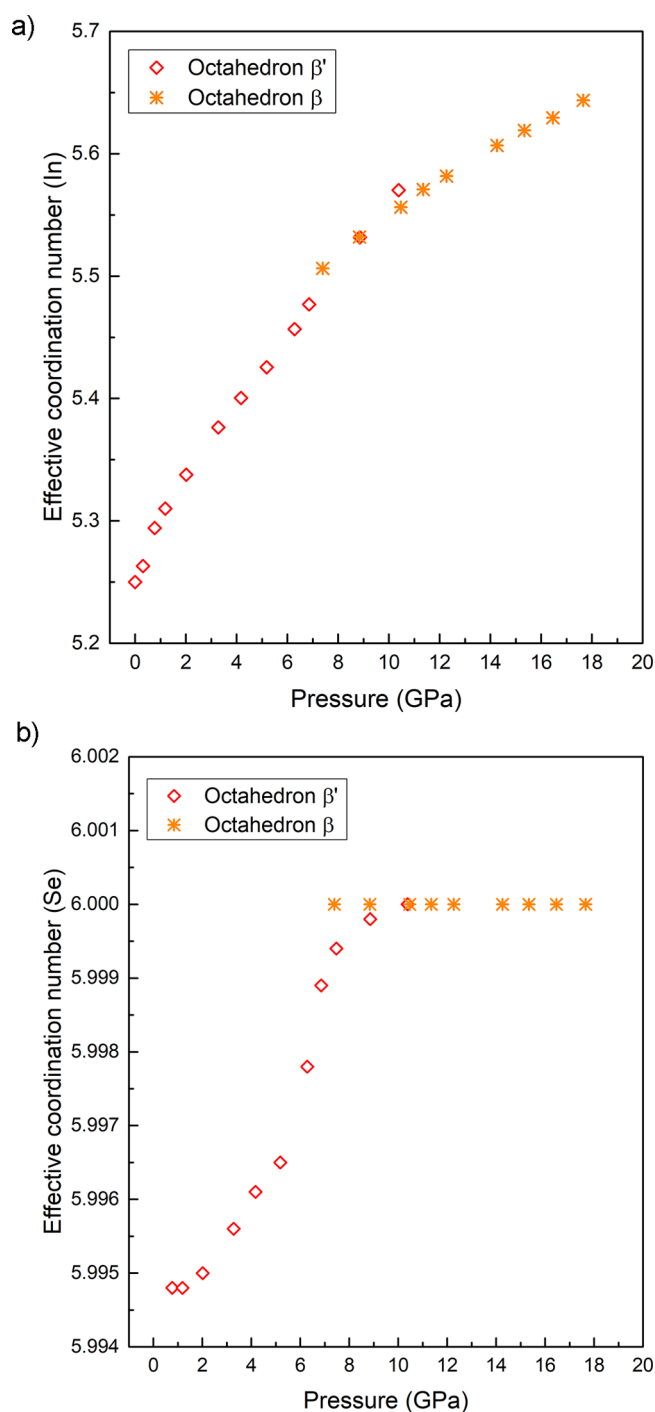


Figure 12. Pressure dependence of the effective coordination index of the octahedron associated with (a) In atom and (b) Se atom in β' (empty rhombus symbol) and β (asterisk symbol) phases.

of pressure-induced phase transitions. Moreover, our study has allowed us to understand that the reason for the discordance in previous measurements is the second-order character of the β' – β phase transition (both phases are energetically very close in a narrow pressure region) and the difficulty to discern between both phases from the experimental point of view. In fact, both our experimental and theoretical techniques clearly indicate that the β' – β phase transition occurs about 10–12 GPa by a gradual symmetrization of the monoclinic β' phase until it reaches a relationship of network parameters that makes the structure rhombohedral (β phase). The changes in the X-

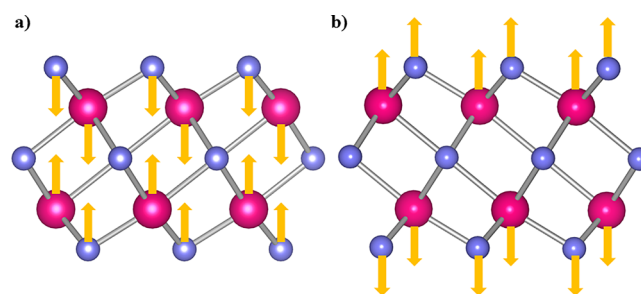


Figure 13. (a) Schematic atomic displacement of the A_g^2 mode of the β' phase. (b) Schematic atomic displacement of the A_g^1 mode of the β phase.

ray diffraction patterns and Raman-active modes during the β' – β phase transition are very subtle and consequently difficult to detect experimentally. That is the reason for the discordance between previous measurements. Furthermore, our Raman results and its comparison to *ab initio* calculations have allowed us to assign most of the modes of the three different phases. We hope the present work will stimulate further experiments at both high pressure and high temperature in order to clarify the thermodynamic equilibrium between β' and β phases.

■ ASSOCIATED CONTENT

§ Supporting Information

The Supporting Information is available free of charge on the ACS Publications website at DOI: 10.1021/acs.inorgchem.8b00778.

XRD powder patterns, Raman spectrum of α phase, Raman spectra of β' phase, downstroke Raman spectra, relaxed Raman spectrum, theoretical infrared and Raman frequencies vs pressure, experimental lattice parameters and unit cell volumes, and effective coordination number (PDF)

■ AUTHOR INFORMATION

Corresponding Author

*E-mail: rovilap@fis.upv.es.

ORCID

Rosario Vilaplana: 0000-0003-0504-2157

Samuel Gallego Parra: 0000-0001-6516-4303

Alejandro Jorge-Montero: 0000-0002-0163-342X

Plácida Rodríguez-Hernández: 0000-0002-4148-6516

Alfonso Munoz: 0000-0003-3347-6518

Daniel Errandonea: 0000-0003-0189-4221

Alfredo Segura: 0000-0002-9979-1302

Francisco Javier Manjón: 0000-0002-3926-1705

Notes

The authors declare no competing financial interest.

■ ACKNOWLEDGMENTS

The authors acknowledge financial support from Spanish government MINECO, the Spanish Agencia Estatal de Investigación (AEI), and Fondo Europeo de Desarrollo Regional (FEDER) under Grants No. MAT2016-75586-C4-1/2/3-P and MAT2015-71070-REDC.

■ REFERENCES

- (1) Ho, C.-H.; Lin, C.-H.; Wang, Y.-P.; Chen, Y.-C.; Chen, S.-H.; Huang, Y.-S. Surface Oxide Effect on Optical Sensing and

Photoelectric Conversion of α - In_2Se_3 Hexagonal Microplates. *ACS Appl. Mater. Interfaces* **2013**, *5*, 2269–2277.

(2) Cui, J.; Liu, X.; Zhang, X.; Li, Y.; Deng, Y. Bandgap reduction responsible for the improved thermoelectric performance of bulk polycrystalline $\text{In}_{2-x}\text{Cu}_x\text{Se}_3$ ($x = 0-0.2$). *J. Appl. Phys.* **2011**, *110*, 023708.

(3) Cui, J.; Zhang, X.; Deng, Y.; Fu, H.; Yan, Y.; Gao, Y.; Li, Y. Modified structures and improved thermoelectric property in Ag-added polycrystalline In_2Se_3 . *Scr. Mater.* **2011**, *64*, 510–512.

(4) Lee, H.; Kang, D.-H.; Tran, L. Indium selenide (In_2Se_3) thin film for phase-change memory. *Mater. Sci. Eng., B* **2005**, *119*, 196–201.

(5) Yu, B.; Ju, S.; Sun, X.; Ng, G.; Nguyen, T. D.; Meyyappan, M.; Janes, D. B. Indium selenide nanowire phase-change memory. *Appl. Phys. Lett.* **2007**, *91*, 133119.

(6) Huang, Y.-T.; Huang, C.-W.; Chen, J.-Y.; Ting, Y.-H.; Lu, K.-C.; Chueh, Y.-L.; Wu, W.-W. Dynamic observation of phase transformation behaviors in indium (III) selenide nanowire based phase change memory. *ACS Nano* **2014**, *8*, 9457–9462.

(7) Li, Q.; Li, Y.; Gao, J.; Wang, S.; Sun, X. High performance single In_2Se_3 nanowire photodetector. *Appl. Phys. Lett.* **2011**, *99*, 243105.

(8) Zhai, T.; Fang, X.; Liao, M.; Xu, X.; Li, L.; Liu, B.; Koide, Y.; Ma, Y.; Yao, J.; Bando, Y. Fabrication of high-quality In_2Se_3 nanowire arrays toward high-performance visible-light photodetectors. *ACS Nano* **2010**, *4*, 1596–1602.

(9) Kwon, S. H.; Ahn, B. T.; Kim, S. K.; Yoon, K. H.; Song, J. Growth of CuIn_3Se_5 layer on CuInSe_2 films and its effect on the photovoltaic properties of $\text{In}_2\text{Se}_3/\text{CuInSe}_2$ solar cells. *Thin Solid Films* **1998**, *323*, 265–269.

(10) Peng, H.; Schoen, D. T.; Meister, S.; Zhang, X. F.; Cui, Y. Synthesis and Phase Transformation of In_2Se_3 and CuInSe_2 Nanowires. *J. Am. Chem. Soc.* **2007**, *129*, 34–35.

(11) Ding, W.; Zhu, J.; Wang, Z.; Gao, Y.; Xiao, D.; Gu, Y.; Zhang, Z.; Zhu, W. Prediction of intrinsic two-dimensional ferroelectrics in In_2Se_3 and other III₂-VI₃ van der Waals materials. *Nat. Commun.* **2017**, *8*, 14956.

(12) Peng, H.; Xie, C.; Schoen, D. T.; Cui, Y. Large anisotropy of electrical properties in layer-structured In_2Se_3 nanowires. *Nano Lett.* **2008**, *8*, 1511–1516.

(13) Sreekumar, R.; Jayakrishnan, R.; Sudha Kartha, C.; Vijayakumar, K.; Khan, S.; Avasthi, D. Enhancement of band gap and photoconductivity in gamma indium selenide due to swift heavy ion irradiation. *J. Appl. Phys.* **2008**, *103*, 023709.

(14) Lin, M.; Wu, D.; Zhou, Y.; Huang, W.; Jiang, W.; Zheng, W.; Zhao, S.; Jin, C.; Guo, Y.; Peng, H. Controlled growth of atomically thin In_2Se_3 flakes by van der Waals epitaxy. *J. Am. Chem. Soc.* **2013**, *135*, 13274–13277.

(15) Wang, Z.; Guo, X.; Li, H.; Wong, T.; Wang, N.; Xie, M. Superlattices of $\text{Bi}_2\text{Se}_3/\text{In}_2\text{Se}_3$: Growth characteristics and structural properties. *Appl. Phys. Lett.* **2011**, *99*, 023112.

(16) Xia, Y.; Qian, D.; Hsieh, D.; Wray, L.; Pal, A.; Lin, H.; Bansil, A.; Grauer, D.; Hor, Y. S.; Cava, R. J. Observation of a large-gap topological-insulator class with a single Dirac cone on the surface. *Nat. Phys.* **2009**, *5*, 398.

(17) Zhang, H.; Liu, C.-X.; Qi, X.-L.; Dai, X.; Fang, Z.; Zhang, S.-C. Topological insulators in Bi_2Se_3 , Bi_2Te_3 and Sb_2Te_3 with a single Dirac cone on the surface. *Nat. Phys.* **2009**, *5*, 438.

(18) Chen, Y.; Analytis, J. G.; Chu, J.-H.; Liu, Z.; Mo, S.-K.; Qi, X.-L.; Zhang, H.; Lu, D.; Dai, X.; Fang, Z. Experimental realization of a three-dimensional topological insulator, Bi_2Te_3 . *Science* **2009**, *325*, 178–181.

(19) Hsieh, D.; Xia, Y.; Qian, D.; Wray, L.; Meier, F.; Dil, J.; Osterwalder, J.; Patthey, L.; Fedorov, A.; Lin, H. Observation of time-reversal-protected single-Dirac-cone topological-insulator states in Bi_2Te_3 and Sb_2Te_3 . *Phys. Rev. Lett.* **2009**, *103*, 146401.

(20) Newman, P. Ordering in AIII₂BVI₃ compounds. *J. Phys. Chem. Solids* **1962**, *23*, 19–23.

(21) Lutz, H.; Fischer, M.; Baldus, H.-P.; Blachnik, R. Zur polymorphie des In_2Se_3 . *J. Less-Common Met.* **1988**, *143*, 83–92.

(22) Pfützner, A.; Lutz, H. Redetermination of the Crystal Structure of γ - In_2Se_3 by Twin Crystal X-Ray Method. *J. Solid State Chem.* **1996**, *124*, 305–308.

(23) Osamura, K.; Murakami, Y.; Tomiie, Y. Crystal Structures of α - and β -Indium Selenide, In_2Se_3 . *J. Phys. Soc. Jpn.* **1966**, *21*, 1848–1848.

(24) Popović, S.; Tonejc, A.; Gržeta-Plenković, B.; Čelustka, B.; Trojko, R. Revised and new crystal data for indium selenides. *J. Appl. Crystallogr.* **1979**, *12*, 416–420.

(25) Han, G.; Chen, Z. G.; Drennan, J.; Zou, J. Indium selenides: structural characteristics, synthesis and their thermoelectric performances. *Small* **2014**, *10*, 2747–2765.

(26) Cui, J.; Wang, L.; Du, Z.; Ying, P.; Deng, Y. High thermoelectric performance of a defect in α - In_2Se_3 -based solid solution upon substitution of Zn for In. *J. Mater. Chem. C* **2015**, *3*, 9069–9075.

(27) Song, Z.; Liu, H.; Du, Z.; Liu, X.; Cui, J. Improvement of thermoelectric performance of α - In_2Se_3 upon S incorporation. *Phys. Status Solidi A* **2016**, *213*, 986–993.

(28) Vassilev, G. P.; Daouchi, B.; Record, M.-C.; Tedenac, J.-C. Thermodynamic studies of the In–Se system. *J. Alloys Compd.* **1998**, *269*, 107–115.

(29) Likforman, A.; Carré, D.; Hillel, R. Structure cristalline du seleniure d'indium In_2Se_3 . *Acta Crystallogr., Sect. B: Struct. Crystallogr. Cryst. Chem.* **1978**, *34*, 1–5.

(30) Kambas, K.; Julien, C.; Jouanne, M.; Likforman, A.; Guittard, M. Raman Spectra of α - and γ - In_2Se_3 . *Phys. Status Solidi B* **1984**, *124*, K105.

(31) Lewandowska, R.; Bacewicz, R.; Filipowicz, J.; Paszkowicz, W. Raman scattering in α - In_2Se_3 crystals. *Mater. Res. Bull.* **2001**, *36*, 2577–2583.

(32) Tao, X.; Gu, Y. Crystalline–crystalline phase transformation in two-dimensional In_2Se_3 thin layers. *Nano Lett.* **2013**, *13*, 3501–3505.

(33) Mafi, E.; Soudi, A.; Gu, Y. Electronically driven amorphization in phase-change In_2Se_3 nanowires. *J. Phys. Chem. C* **2012**, *116*, 22539–22544.

(34) Island, J. O.; Blanter, S. I.; Buscema, M.; van der Zant, H. S. J.; Castellanos-Gomez, A. Gate Controlled Photocurrent Generation Mechanisms in High-Gain In_2Se_3 Phototransistors. *Nano Lett.* **2015**, *15*, 7853–7858.

(35) Wu, D.; Pak, A. J.; Liu, Y.; Zhou, Y.; Wu, X.; Zhu, Y.; Lin, M.; Han, Y.; Ren, Y.; Peng, H. Thickness-Dependent Dielectric Constant of Few-Layer In_2Se_3 Nanoflakes. *Nano Lett.* **2015**, *15*, 8136–8140.

(36) Zhou, Y.; Wu, D.; Zhu, Y.; Cho, Y.; He, Q.; Yang, X.; Herrera, K.; Chu, Z.; Han, Y.; Downer, M. C. Out-of-Plane Piezoelectricity and Ferroelectricity in Layered α - In_2Se_3 Nanoflakes. *Nano Lett.* **2017**, *17*, 5508–5513.

(37) Van Landuyt, J.; Van Tendeloo, G.; Amelinckx, S. Phase transitions in In_2Se_3 as studied by electron microscopy and electron diffraction. *Phys. Status Solidi A* **1975**, *30*, 299–314.

(38) Manolikas, C. New results on the phase transformations of In_2Se_3 . *J. Solid State Chem.* **1988**, *74*, 319–328.

(39) Zhao, J.; Yang, L. Structure evolutions and metallic transitions in In_2Se_3 under high pressure. *J. Phys. Chem. C* **2014**, *118*, 5445–5452.

(40) Manjón, F. J.; Vilaplana, R.; Gomis, O.; Pérez-González, E.; Santamaría-Pérez, D.; Marín-Borrás, V.; Segura, A.; González, J.; Rodríguez-Hernández, P.; Munoz, A. High-pressure studies of topological insulators Bi_2Se_3 , Bi_2Te_3 , and Sb_2Te_3 . *Phys. Status Solidi B* **2013**, *250*, 669–676.

(41) Vilaplana, R.; Sans, J. A.; Manjón, F. J.; Andrada-Chacón, A.; Sánchez-Benítez, J.; Popescu, C.; Gomis, O.; Pereira, A.; García-Domene, B.; Rodríguez-Hernández, P. Structural and electrical study of the topological insulator SnBi_2Te_4 at high pressure. *J. Alloys Compd.* **2016**, *685*, 962–970.

(42) Rasmussen, A. M.; Teklemichael, S. T.; Mafi, E.; Gu, Y.; McCluskey, M. D. Pressure-induced phase transformation of In_2Se_3 . *Appl. Phys. Lett.* **2013**, *102*, 062105.

- (43) Ke, F.; Liu, C.; Gao, Y.; Zhang, J.; Tan, D.; Han, Y.; Ma, Y.; Shu, J.; Yang, W.; Chen, B. Interlayer-glide-driven isosymmetric phase transition in compressed In_2Se_3 . *Appl. Phys. Lett.* **2014**, *104*, 212102.
- (44) Ke, F.; Dong, H.; Chen, Y.; Zhang, J.; Liu, C.; Zhang, J.; Gan, Y.; Han, Y.; Chen, Z.; Gao, C. Decompression-Driven Superconductivity Enhancement in In_2Se_3 . *Adv. Mater.* **2017**, *29*, 1701983.
- (45) Rasmussen, A. M.; Mafi, E.; Zhu, W.; Gu, Y.; McCluskey, M. D. High pressure γ -to- β phase transition in bulk and nanocrystalline In_2Se_3 . *High Pressure Res.* **2016**, *36*, 549–556.
- (46) Vilaplana, R.; Gomis, O.; Manjón, F. J.; Ortiz, H.; Pérez-González, E.; López-Solano, J.; Rodríguez-Hernández, P.; Muñoz, A.; Errandonea, D.; Ursaki, V. Lattice dynamics study of HgGa_2Se_4 at high pressures. *J. Phys. Chem. C* **2013**, *117*, 15773–15781.
- (47) Piermarini, G.; Block, S.; Barnett, J. Hydrostatic limits in liquids and solids to 100 kbar. *J. Appl. Phys.* **1973**, *44*, 5377–5382.
- (48) Klotz, S.; Chervin, J. C.; Munsch, P.; Marchand, G. L. Hydrostatic limits of 11 pressure transmitting media. *J. Phys. D: Appl. Phys.* **2009**, *42*, 075413.
- (49) Fauth, F.; Peral, I.; Popescu, C.; Knapp, M. The new material science powder diffraction beamline at ALBA synchrotron. *Powder Diffr.* **2013**, *28*, S360–S370.
- (50) Hammersley, A.; Svensson, S.; Hanfland, M.; Fitch, A.; Hausermann, D. Two-dimensional detector software: from real detector to idealised image or two-theta scan. *High Pressure Res.* **1996**, *14*, 235–248.
- (51) Toby, B. H. EXPGUI, a graphical user interface for GSAS. *J. Appl. Crystallogr.* **2001**, *34*, 210–213.
- (52) Dewaele, A.; Loubeyre, P.; Mezouar, M. Equations of state of six metals above 94 GPa. *Phys. Rev. B: Condens. Matter Mater. Phys.* **2004**, *70*, 094112.
- (53) Syassen, K. Ruby under pressure. *High Pressure Res.* **2008**, *28*, 75–126.
- (54) Hohenberg, P.; Kohn, W. Inhomogeneous electron gas. *Phys. Rev.* **1964**, *136*, B864.
- (55) Mujica, A.; Rubio, A.; Munoz, A.; Needs, R. High-pressure phases of group-IV, III–V, and II–VI compounds. *Rev. Mod. Phys.* **2003**, *75*, 863.
- (56) Kresse, G.; Furthmüller, J. Efficient iterative schemes for ab initio total-energy calculations using a plane-wave basis set. *Phys. Rev. B: Condens. Matter Mater. Phys.* **1996**, *54*, 11169.
- (57) Blöchl, P. E. Projector augmented-wave method. *Phys. Rev. B: Condens. Matter Mater. Phys.* **1994**, *50*, 17953.
- (58) Perdew, J. P.; Burke, K.; Ernzerhof, M. Pressure and Temperature Dependence of the Lattice Dynamics of CuAlO_2 Investigated by Raman Scattering Experiments and Ab Initio Calculations [J]. *Phys. Rev. Lett.* **1996**, *77*, 1.
- (59) Nielsen, O.; Martin, R. M. Quantum-mechanical theory of stress and force. *Phys. Rev. B: Condens. Matter Mater. Phys.* **1985**, *32*, 3780.
- (60) Parlinski, K. Computer Code Phonon. <http://wolf.ifj.edu.pl/phonon/>.
- (61) Errandonea, D.; Kumar, R.; Gomis, O.; Manjón, F. J.; Ursaki, V.; Tiginyanu, I. X-ray diffraction study on pressure-induced phase transformations and the equation of state of ZnGa_2Te_4 . *J. Appl. Phys.* **2013**, *114*, 233507.
- (62) Gleissner, J.; Errandonea, D.; Segura, A.; Pellicer-Porres, J.; Hakeem, M.; Proctor, J.; Raju, S.; Kumar, R.; Rodríguez-Hernández, P.; Muñoz, A. Monazite-type SrCrO_4 under compression. *Phys. Rev. B: Condens. Matter Mater. Phys.* **2016**, *94*, 134108.
- (63) Errandonea, D.; Kumar, R.; Achary, S.; Gomis, O.; Manjón, F. J.; Shukla, R.; Tyagi, A. New high-pressure phase and equation of state of $\text{Ce}_2\text{Zr}_2\text{O}_8$. *J. Appl. Phys.* **2012**, *111*, 053519.
- (64) Errandonea, D. Landau theory applied to phase transitions in calcium orthotungstate and isostructural compounds. *Europhys. Lett.* **2007**, *77*, S6001.
- (65) Errandonea, D.; Martínez-García, D.; Segura, A.; Haines, J.; Machado-Charry, E.; Canadell, E.; Chervin, J.; Chevy, A. High-pressure electronic structure and phase transitions in monoclinic InSe : X-ray diffraction, Raman spectroscopy, and density functional theory. *Phys. Rev. B: Condens. Matter Mater. Phys.* **2008**, *77*, 045208.
- (66) Weszka, J.; Daniel, P.; Burian, A.; Burian, A.; Nguyen, A. Raman scattering in In_2Se_3 and InSe_2 amorphous films. *J. Non-Cryst. Solids* **2000**, *265*, 98–104.
- (67) Momma, K.; Izumi, F. VESTA 3 for three-dimensional visualization of crystal, volumetric and morphology data. *J. Appl. Crystallogr.* **2011**, *44*, 1272–1276.
- (68) Robinson, K.; Gibbs, G.; Ribbe, P. Quadratic elongation: a quantitative measure of distortion in coordination polyhedra. *Science* **1971**, *172*, 567–570.
- (69) Hoppe, R. Effective coordination numbers (ECoN) and mean fictive ionic radii (MEFIR). *Zeitschrift für Kristallographie-Crystalline Materials* **1979**, *150*, 23–52.
- (70) Hoppe, R.; Voigt, S.; Glaum, H.; Kissel, J.; Müller, H. P.; Bernet, K. A new route to charge distributions in ionic solids. *J. Less-Common Met.* **1989**, *156*, 105–122.
- (71) Jmol: an open-source Java viewer for chemical structures. <http://jmol.sourceforge.net>.